Combining Electronic Structure Methods with the Calculation of Hydrogen Vibrational Wavefunctions: Application to Hydride Transfer in Liver Alcohol Dehydrogenase

Simon P. Webb, Pratul K. Agarwal, and Sharon Hammes-Schiffer*

Department of Chemistry, The Pennsylvania State University, 152 Davey Laboratory, University Park, PA 16802

This paper presents an application of a computational approach combining electronic structure methods with the calculation of hydrogen vibrational wavefunctions. This application is directed at elucidating the nature of the nuclear quantum mechanical effects in the oxidation of benzyl alcohol catalyzed by liver alcohol dehydrogenase (LADH). The hydride transfer from the benzyl alcohol substrate to the NAD^+ cofactor is described by a 148-atom model of the active site. The hydride potential energy curves and the associated hydrogen vibrational wavefunctions are calculated for structures along minimum energy paths and straight-line reaction paths obtained from electronic structure calculations at the semiempirical PM3 and ab initio RHF/3-21G levels. The results indicate that, for these levels of theory, the hydride transfer is adiabatic and hydrogen tunneling does not play a critical role along the minimum energy path. In contrast, nonadiabatic effects and hydrogen tunneling are shown to be important along the more relevant straight-line reaction paths. The secondary hydrogens were found to be significantly coupled to the transferring hydride near the transition state. In addition, the puckering of the NAD^+ ring was found to be a dominant contribution to the reaction coordinate near the transition state. Further from the transition state, the reaction coordinate is a mixture of many heavy-atom modes, including the donor−acceptor distance and the distance between the substrate and the neighboring zinc and serine residue. These results imply that hydrogen tunneling in LADH is strongly impacted by the puckering of the NAD^+ ring (which modulates the asymmetry of the hydride potential energy curve) and the distance between the donor and acceptor carbons (which modulates the barrier of the hydride potential energy curve).

I. Introduction

Kinetic isotope effect experiments indicate that nuclear quantum effects are significant in hydrogen transfer reactions catalyzed by alcohol dehydrogenases.[1–5] A number of different experimental approaches have been used to probe the role of hydrogen tunneling in these enzyme reactions.[4] These approaches include the investigation of the temperature dependence of isotope effects and the use of exponential relationships among hydrogen, deuterium, and tritium isotope effects (at both primary and secondary positions). In the interpretation of these experiments, hydrogen tunneling is implicated by deviations from semiclassical predictions based on zero point energies.[4]

Several theoretical studies have addressed the issue of hydrogen quantum effects in alcohol dehydrogenases and related systems. Kreevoy, Truhlar, and co-workers studied hydrogen tunneling effects for hydride transfer among a series of NAD^+ analogues.[6,7] They constructed an experimentally based family of potential energy surfaces and calculated reaction rates and kinetic isotope effects using variational transition state theory in conjunction with semiclassical tunneling calculations. Their results indicate that tunneling is significant in these hydride transfer reactions. Warshel and co-workers combined a centroid path integral treatment with an empirical valence bond potential to simulate NADH hydride transfer in solution and in lactate dehydrogenase.[8,9] A different approach has been pursued by Bruno and Bialek,[10] who emphasize the importance of thermal fluctuations of the enzyme in mediating hydrogen tunneling.

They incorporated vibrational coupling into a semiempirical model for predicting the temperature dependence of the kinetic isotope effects. More recently, Klinman and co-workers developed a simple computational model to fit the experimental kinetic isotope effect results for yeast alcohol dehydrogenase.[11] Their model includes both substantial hydrogen tunneling and coupling between the reaction coordinate and a large number of vibrational modes.

In this paper, we investigate the nuclear quantum effects for hydride transfer in liver alcohol dehydrogenase (LADH) through a combination of electronic structure and hydrogen vibrational wavefunction calculations. The basic approach is to calculate the hydride potential energy curves and the associated hydrogen vibrational wavefunctions for structures along a reaction path obtained from electronic structure calculations. The shape of the hydride potential energy curve is determined by the geometry of the entire system and thus changes along the reaction path. The hydride potential energy curves and the associated hydrogen vibrational wavefunctions provide useful information about the fundamental nature of the nuclear quantum effects.[13] For example, Figure 1 is a schematic illustration of one-dimensional hydrogen vibrational wavefunctions along two different reaction paths. In Figure 1a, the hydride transfer is a tunneling process since the lowest two adiabatic vibrational states are below the barrier in the transition state. The extent of tunneling is determined by the tunnel splitting (i.e., the energy separation between the adiabatic hydrogen vibrational states in the transition state). In contrast, in Figure 1b the hydride transfer is no longer tunneling since the lowest adiabatic vibrational state is
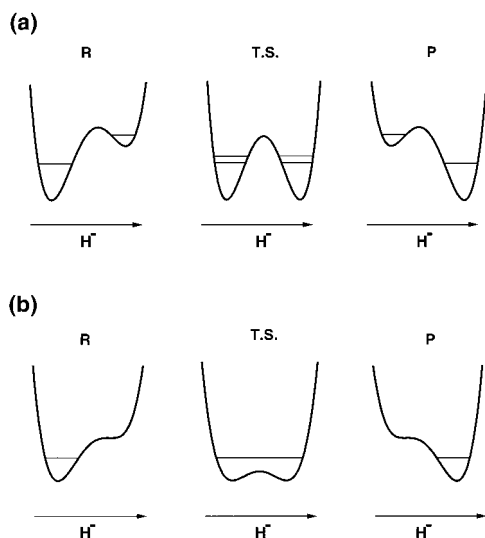
* Corresponding author. E-mail: shs@chem.psu.edu.

Figure 1. Schematic illustration of the one-dimensional hydride potential energy curves for two different reaction paths. The curves are functions of the one-dimensional hydride coordinate, and R, T. S., and P correspond to the reactant, transition state, and product configurations, respectively. (a) depicts hydride tunneling (i.e., the lowest two adiabatic vibrational states are below the barrier in the T. S.), and (b) depicts hydride transfer without tunneling (i.e., the lowest adiabatic vibrational state is above the barrier in the T. S.). Note that the intermediate configurations labeled T. S. need not be true transition states.
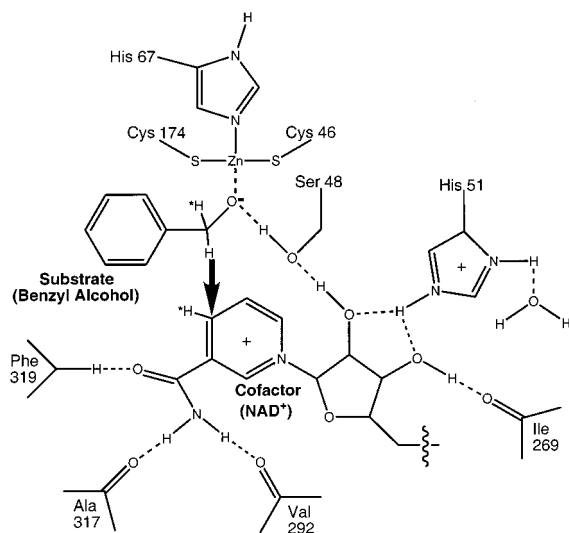

Figure 2. Schematic illustration of the active site of LADH with a benzyl alkoxide substrate and an NAD$^+$ cofactor. The dark arrow indicates the hydride transfer reaction. The asterisks denote the secondary hydrogen atoms involved in the hydride transfer reaction.

above the barrier in the transition state. Nevertheless, even in this case the hydride transfer is still very much quantum mechanical in character. (Note that the intermediate configurations in Figure 1 need not be true transition states.) Thus, an analysis of the hydrogen vibrational wavefunctions along reaction paths provides insight into the nuclear quantum effects. Moreover, an analysis of the geometries and molecular orbitals along the reaction path provides information about the important contributions to the reaction coordinate and the factors influencing hydrogen tunneling.

We analyze the hydride potential energy curves and the associated hydrogen vibrational wavefunctions along both the minimum energy path (MEP) and straight-line reaction paths generated from points along the MEP. The MEP is defined as

the steepest descent path in mass-weighted coordinates from the transition state down toward reactants and toward products. As discussed throughout the literature,[14,15] however, typically hydrogen transfer reactions have MEPs with large curvature due to the masses involved when a light particle is transferred between two heavy ones. When the MEP has large curvature, the relevant dynamical motion deviates far from this path. Thus, the MEP may not provide the most useful description for hydrogen transfer reactions. As shown previously,[15,16] a more relevant reaction path for reactions with large curvature is the straight-line reaction path, which is defined as the linear interpolation (in mass-weighted coordinates) between geometries on the reactant and product sides of the MEP. The MEP and straight-line reaction path form the basis of the semiclassical tunneling approximations developed by Truhlar and co-workers,[14,16] where the MEP is used in the zero- and small-curvature approximations and the straight-line reaction paths are used in the large-curvature approximations. In contrast to these semiclassical tunneling approximations, our approach is not designed to calculate quantitatively accurate rates or kinetic isotope effects. Instead, our approach is designed to provide valuable insight into the fundamental nature of the nuclear quantum effects, including the significance of hydrogen tunneling and zero point energy, the role of secondary hydrogens, and the dominant contributions to the reaction coordinate for these various paths. This approach also elucidates the factors that impact hydrogen tunneling.

This paper presents the application of this methodology to the oxidation of benzyl alcohol by horse liver alcohol dehydrogenase (HLADH). In section II, we describe the methods utilized for the electronic structure and the hydrogen vibrational wavefunction calculations. In section III, we present the results of the application of this methodology to hydride transfer in HLADH. Section IV summarizes both the advantages of this computational approach and the insight gained from the application to HLADH.

II. Methods

A. Electronic Structure Calculations. Electronic structure calculations were carried out using the semiempirical PM3 method and the Restricted Hartree−Fock (RHF) method with the double-ζ quality basis set 3-21G.[17−19] This split-valence basis set was previously found to give reasonable structures for the system under study.[12] These calculations were used to investigate the hydride transfer reaction in a 148-atom model of the active site of LADH depicted in Figure 2. This model includes analogues of nine protein residues (Cys46, Ser48, His51, His67, Cys174, Ile269, Val292, Ala317 and Phe319), the catalytic zinc ion, the substrate benzyl alcohol, a coenzyme NAD$^+$ analogue, and a water molecule. The water molecule was included to prevent the His51 ring from flipping. The hydrophobic side chains of protein residues that do not participate in the reaction were truncated to reduce the number of atoms in the model. The analogues used for the amino acids and coenzyme in this model are depicted in Figure 3. The overall charge for this model is +1. Note that this enzyme reaction involves both the deprotonation of the alcohol substrate (which is thought to occur by a proton relay) and a hydride transfer from the substrate to an NAD$^+$ cofactor. In a previous paper,[12] we presented electronic structure calculations and classical molecular dynamics simulations indicating that alcohol deprotonation occurs prior to hydride transfer. Based on these previous results, this paper focuses only on the hydride transfer reaction after deprotonation of the alcohol, as shown in Figure 2.
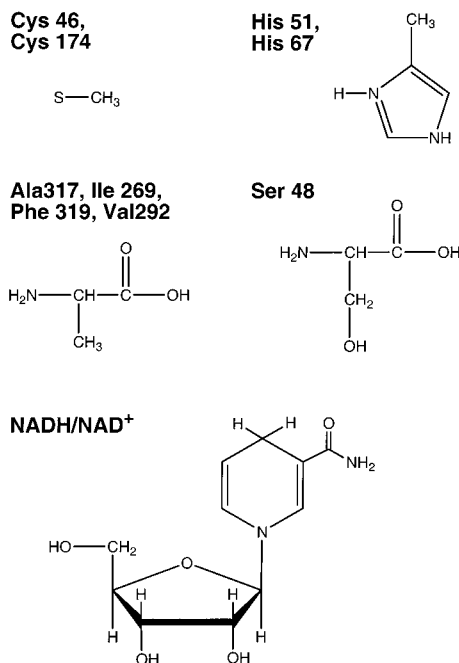
Cys 46,
Cys 174

S—CH₃

His 51,
His 67

Ala317, Ile 269,
Phe 319, Val292

Ser 48

NADH/NAD⁺

Figure 3. Analogues for the amino acids and the NAD⁺ coenzyme used in the 148-atom model of the LADH active site depicted in Figure 2. His67 is deprotonated in this model.

In ref 12 we presented the results of electronic structure calculations at the PM3 and RHF/3-21G levels on this model. The minimum energy path (MEP) for the hydride transfer reaction was generated at the PM3 level using the intrinsic reaction coordinate (IRC) method of Gonzales and Schlegel.[20] In addition, the reactant, transition state, and product structures were found at the RHF/3-21G level of theory. In the present paper, an approximate Hessian (energy second derivative) generated during the previous RHF/3-21G transition state geometry search was used to initiate the generation of a portion of the hydride transfer MEP at the RHF/3-21G level. The approximate Hessian was used due to the excessive computational cost of calculating an exact Hessian for this system. Structures from the PM3 and RHF/3-21G MEPs were selected for examination of nuclear quantum effects using methodology described below. Furthermore, to investigate the role of secondary hydrogens in the hydride transfer reaction, constrained RHF/3-21G geometry optimizations, in which all atoms are frozen except the secondary hydrogens, were carried out. Interpretation of the electronic wavefunctions resulting from the RHF/3-21G electronic structure calculations was aided by the localization of molecular orbitals (LMOs) using the Boys method.[21]

All electronic structure calculations were carried out using the electronic structure package GAMESS[22] except for the constrained geometry optimizations, which were carried out with Gaussian98.[23] All energy and energy gradient convergence criteria used were program defaults. It should be noted, however, that the RHF/3-21G transition state geometry found in the previous study[12] and used in this one satisfied a relaxed energy gradient criterion of a maximum of 0.001 Hartree/Bohr and an RMS of one-third of this.

B. Hydrogen Wavefunction Calculations. Hydrogen vibrational wavefunctions were calculated using the FGH-MCSCF (Fourier grid Hamiltonian multiconfigurational self-consistent-field) methodology.[24] In the FGH-MCSCF method, the potential energy surface for the transferring hydrogen is calculated on a grid (i.e., all nuclei except the transferring hydrogen are fixed, and the energy is calculated for the hydrogen positioned at each

point on the grid). The hydrogen vibrational wavefunctions are calculated by numerically solving the time-independent Schrödinger equation for the hydrogen nucleus moving on this potential energy surface. The MCSCF approach is utilized to avoid diagonalization of large matrixes for the calculation of multidimensional wavefunctions. In the one-dimensional case, the method becomes equivalent to the Fourier grid Hamiltonian method of Marston and Balint-Kurti.[25]

In the present implementation, for one-dimensional wavefunctions the one-dimensional grid is always along the axis defined by the donor and acceptor atoms and is centered between them. For the LADH system, this axis is defined by the donor (substrate) and acceptor (NAD⁺) carbon atoms, denoted C_D and C_A, respectively. For three-dimensional wavefunctions, two additional grid axes are defined that are equal in length and perpendicular to the first axis (and also perpendicular to each other). Grid spacing in all dimensions is the same and evenly spaced.

Hydrogen wavefunctions were calculated at specified points on the PM3 and RHF/3-21G MEPs. Both one-dimensional and three-dimensional wavefunctions were calculated at the PM3 level; only one-dimensional hydrogen vibrational wavefunctions were calculated at the RHF/3-21G level. Hydrogen wavefunctions were also calculated for specified points along straight-line reaction paths at the PM3 and RHF/3-21G levels. These straight-line reaction paths were generated between points of approximately equal energy on the reactant and product sides of the MEPs. For reactant and product points with mass-weighted Cartesian coordinates $\mathbf{x}_r$ and $\mathbf{x}_p$, respectively, the straight-line reaction path is defined as[15]

$$\mathbf{x}_o(s) = \frac{1}{2}(\mathbf{x}_r + \mathbf{x}_p) + (\mathbf{x}_p - \mathbf{x}_r)(s/\Delta s) \qquad (1)$$

where $\Delta s = |\mathbf{x}_p - \mathbf{x}_r|$. (Note that the vectors $\mathbf{x}_o$, $\mathbf{x}_r$, and $\mathbf{x}_p$ include the coordinates of all nuclei in the system.)

The calculation of the hydrogen vibrational wavefunctions required the generation of a grid potential for the hydrogen (as described above) for the structures at these points. Automated generation of these grids was achieved by interfacing the FGH-MCSCF method with the electronic structure package GAMESS.[22] Convergence tests performed with PM3 one-dimensional hydrogen vibrational wavefunctions indicated that qualitatively adequate wavefunction energies for the first few states are obtained with as few as 16 points per dimension and a grid length of 1.6 Å. More points were used wherever computationally feasable. The number of grid points per dimension and the grid length chosen for the calculations in this paper are (1) PM3 one-dimensional: 64 grid points, 2.4 Å; (2) PM3 three-dimensional: 16 grid points, 1.6 Å; and (3) RHF/3-21G one-dimensional: 32 grid points, 1.6 Å.

III. Results and Discussion

We calculated the hydrogen vibrational wavefunctions for structures on the MEP and for structures on a straight-line reaction path generated from points along the MEP at the PM3 and the RHF/3-21G levels. As shown in ref 12, the geometries and energies obtained at the PM3 level are somewhat unreliable for this system. Furthermore, the PM3 method is parametrized to already include some of the zero point energy effects. The RHF/3-21G method provides more reliable geometries without these additional complications. Moreover, previously[12] we found that the barrier height and endothermicity obtained at the DFT/B3LYP/6-31G** level for the RHF/3-21G geometries (21.9 and

Calculation of Hydrogen Vibrational Wavefunctions

J. Phys. Chem. B, Vol. 104, No. 37, 2000 **8887**

TABLE 1: Zero Point Energies Calculated at the PM3 and RHF/3-21G Levels for the Following Structures: Reactant (R), R*, Transition State (T.S.), P*, and Product (P)[a]

	PM3		RHF/3-21G
	1-D Grid	3-D Grid	1-D Grid
R	3.8	6.9	–
R*	2.8	5.7	2.9
T.S.	1.4	4.9	2.1
P*	2.7	6.1	3.0
P	3.8	7.3	–

[a] The values at the PM3 level are given for both one-dimensional and three-dimensional hydrogen vibrational wavefunctions, while the values at the RHF/3-21G level are given for only one-dimensional hydrogen wavefunctions. The zero point energy is defined to be the difference in energy of the lowest hydrogen vibrational state and the lowest-energy point on the hydride potential energy curve. R* and P* are defined in Figures 4 and 9. All values are given in kcal/mol.
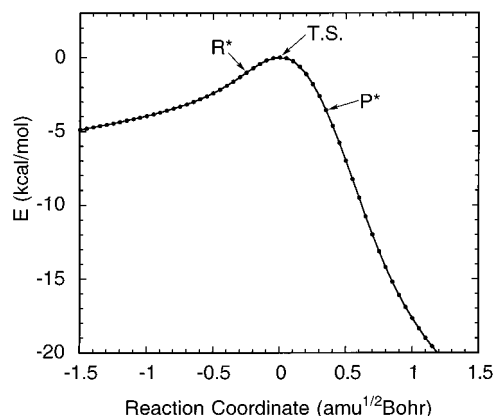

Figure 4. A portion of the minimum energy path for hydride transfer calculated with the semiempirical PM3 method. The three points corresponding to the structures R*, T. S., and P* are indicated.

4.9 kcal/mole, respectively) agree qualitatively with the experimental[26] free energies of activation and reaction (15 and 1 kcal/mole, respectively). On the other hand, we were able to calculate three-dimensional hydrogen vibrational wavefunctions at the PM3 level but not at the RHF/3-21G level due to computational limitations. Thus, first we present the PM3 results to provide preliminary insight into the qualitative aspects of nuclear tunneling for this system. Subsequently, we present the RHF/3-21G results with a more detailed analysis.

The portion of the MEP obtained with PM3 near the transition state for the hydride transfer step is shown in Figure 4. For comparison, the energies of the optimized reactant and product structures are −17.4 kcal/mol and −63.3 kcal/mol, respectively, relative to the transition state (T. S.) energy. Note that at the PM3 level the MEP is quite asymmetric, in contrast to the RHF/3-21G results that are presented below.

The hydrogen vibrational wavefunctions were obtained for the structures corresponding to the three points R*, T. S., and P* denoted in Figure 4. The corresponding zero point energies are given in Table 1. The one-dimensional hydride potential energy curves along the C_D-C_A axis and the corresponding hydrogen vibrational wavefunctions for the three structures R*, T. S., and P* along the MEP are shown in Figure 5. (The origin is at the midpoint between the two carbon atoms.) Figure 5a depicts the hydrogen vibrational wavefunctions for structure R* and shows that the ground state hydrogen vibrational wavefunction is localized near the donor carbon C_D. Similarly, Figure 5c depicts the hydrogen vibrational wavefunctions for structure P* and shows that the ground state hydrogen vibrational wavefunction is localized near the acceptor carbon C_A. Figure
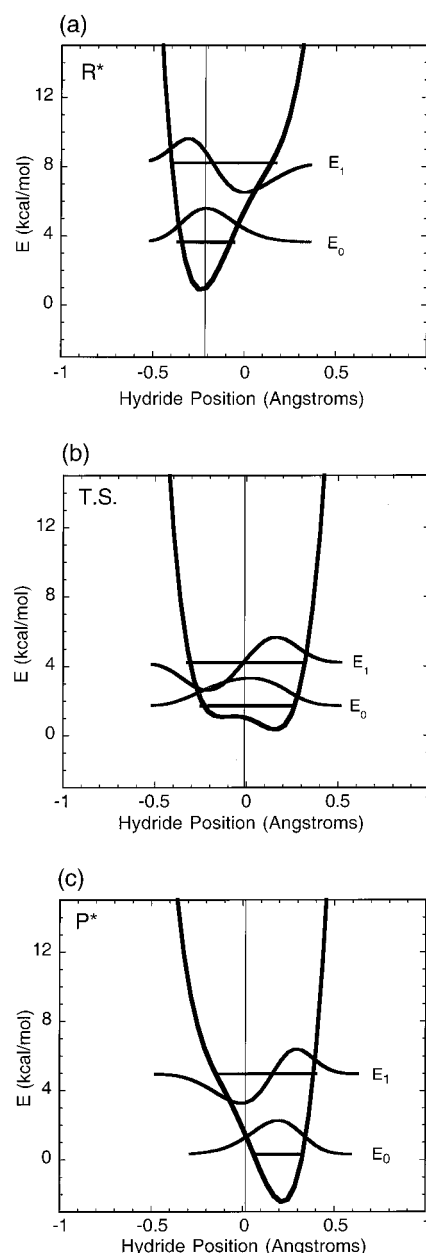

Figure 5. One-dimensional hydride potential energy curves obtained with the PM3 semiempirical method and the corresponding one-dimensional hydrogen vibrational wavefunctions for the (a) R*, (b) T. S., and (c) P* structures defined in Figure 4. Both the ground and first excited hydride vibrational wavefunctions with energies E_0 and E_1, respectively, are shown. The vertical lines denote the position of the projected classical hydride in the MEP structures.

5b depicts the hydrogen vibrational wavefunctions for the transition state structure. For this structure, the potential energy curve exhibits a very low barrier, but the lowest energy vibrational state is above this barrier and is delocalized between the donor and acceptor carbon atoms. The hydrogen vibrational wavefunctions depicted in this figure suggest that the reaction is vibrationally adiabatic (i.e., the hydride transfer reaction occurs on the ground hydrogen vibrational state) and that hydride tunneling is not significant along the MEP. (Compare this to the schematic illustrations of hydride transfer in Figure 1.)

Figure 5 illustrates the significance of three-dimensional hydride motion and nuclear quantum effects for the generation of the MEP. The vertical lines in Figure 5 denote the position of the classical hydride projected onto the C_D-C_A axis. The
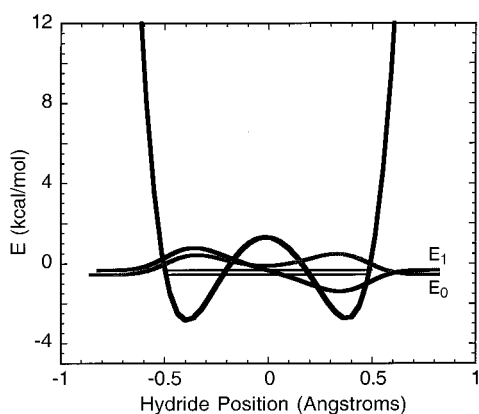
Figure 6. One-dimensional hydride potential energy curve obtained at the PM3 level and the corresponding one-dimensional hydrogen vibrational wavefunctions for a point along the straight-line reaction path connecting structures $\bar{R}$ and $\bar{P}$ defined in the text. The point was chosen so that the hydride potential energy curve is symmetric. Both the ground and first excited hydride vibrational wavefunctions with energies E_0 and E_1, respectively, are shown.

energy scale is chosen so that zero energy of the ordinate ($E = 0$) represents the energy of the corresponding structure obtained from the PM3 minimum energy path. If the hydride moved in only one dimension along the C_D-C_A axis, the vertical line would intersect the hydride potential energy curve at zero energy ($E = 0$). This is not the case for any of the curves in Figure 5 due to the three-dimensional motion of the hydride during the calculation of the MEP. Furthermore, the discrepancies between the vertical line and the center of the hydrogen vibrational wavefunction indicate that the MEP obtained with a classical hydride is problematic. A better description would be to average the gradients for the other atoms over the hydride wavefunction during the generation of the MEP. This is a direction for future research.

As discussed in the Introduction, hydrogen transfer reactions are expected to deviate from the MEP due to the large curvature of the MEP. Thus, we also investigated straight-line reaction paths generated by linear interpolation between structures on the reactant and product sides of the MEP. We found that the straight-line reaction path connecting the reactant and product minima resulted in nonphysical structures due to substantial geometrical differences at the periphery of the 148-atom model system. (Note that for such a large system, the hydride vibrational mode is not expected to be a dominant contribution to the reaction coordinate near the reactant and product minima.) To obtain physically reasonable reaction paths, we generated straight-line paths between two approximately equal energy structures on the reactant and product sides of the MEP. Here, we present the results from the straight-line reaction path connecting the two structures corresponding to the points $\bar{R}$ and $\bar{P}$ with reaction coordinates $s = -26.0$ amu$^{1/2}$ Bohr and $s = 0.9$ amu$^{1/2}$ Bohr, respectively, relative to the transition state shown in Figure 4. These points are not shown on this figure but are included in the complete minimum energy path presented in ref 12. The C_D-C_A distances are 3.73 and 2.85 Å, respectively, for the $\bar{R}$ and $\bar{P}$ structures. The hydride potential energy curve and the corresponding hydrogen vibrational wavefunction at a point along this straight-line reaction path are depicted in Figure 6. The point was chosen so that the hydride potential energy curve was symmetric. The C_D-C_A distance for the structure at this point is 3.16 Å, which is significantly longer than the C_D-C_A distance of 2.84 Å for the transition state along the MEP. The longer C_D-C_A distance leads to a higher barrier along the hydride coordinate. As a result,
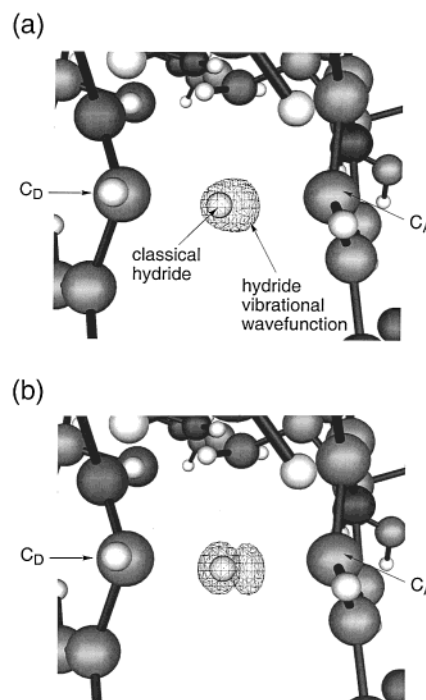

Figure 7. Three-dimensional hydrogen vibrational wavefunctions obtained with the PM3 semiempirical method for the T. S. along the MEP. (a) depicts the ground and (b) depicts the first excited hydride vibrational wavefunction. The positions of the classical hydride are also indicated. The contour value of the surfaces is 0.02 Bohr$^{3/2}$.

for this structure the lowest two vibrational states are below the barrier with a tunnel splitting of 0.22 kcal/mol. The tunnel splitting is expected to decrease as the C_D-C_A distance increases. Thus, for this straight-line reaction path, nonadiabatic effects and hydride tunneling are expected to play important roles.

We emphasize that our goal in presenting the hydride wavefunction for a point along a straight-line reaction path is to illustrate that the nuclear quantum effects may be qualitatively different for the actual reaction path than for the MEP. The specific straight-line reaction path described here is arbitrary and is used only as an example of a reasonable alternative path to the MEP. The actual reaction path for this model system cannot be obtained with standard electronic structure methods. For the biological system, the reaction path will be determined by dynamical fluctuations of the enzyme.

The three-dimensional hydrogen vibrational wavefunctions obtained at the PM3 level for the transition state along the MEP and for a point along the straight-line reaction path described above are shown in Figures 7 and 8, respectively. As for the one-dimensional wavefunctions, the classical hydride is not located at the center of the hydrogen vibrational wavefunction. Figure 7a illustrates that the ground state hydrogen vibrational wavefunction for the transition state is almost spherical. The irregularity of the shape is due to the asymmetry of the environment. The first excited hydrogen vibrational wavefunction has a node between two adjacent lobes (postive and negative phase), as expected for the first excited state of an approximately harmonic potential. In contrast, Figure 8a illustrates that the ground state hydrogen vibrational wavefunction at the point along the straight-line reaction path consists of two lobes of the same phase, indicating a delocalization of the hydrogen vibrational wavefunction over an approximately symmetric double well potential. As expected, the first excited hydrogen vibrational wavefunction has a node between two separated lobes of opposite phase. The tunnel splitting for this
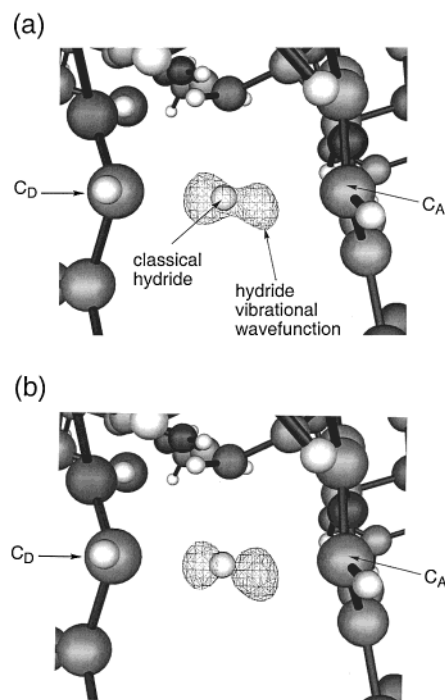
Calculation of Hydrogen Vibrational Wavefunctions

J. Phys. Chem. B, Vol. 104, No. 37, 2000 **8889**

Figure 8. Three-dimensional hydrogen vibrational wavefunctions obtained with the PM3 semiempirical method for a point along the straight-line reaction path connecting structures $\bar{R}$ and $\bar{P}$ defined in the text (where the point was chosen to obtain a hydrogen vibrational wavefunction with two lobes). (a) depicts the ground and (b) depicts the first excited hydride vibrational wavefunction. The positions of the classical hydride are also indicated. The contour value of the surfaces is 0.02 Bohr$^{3/2}$.
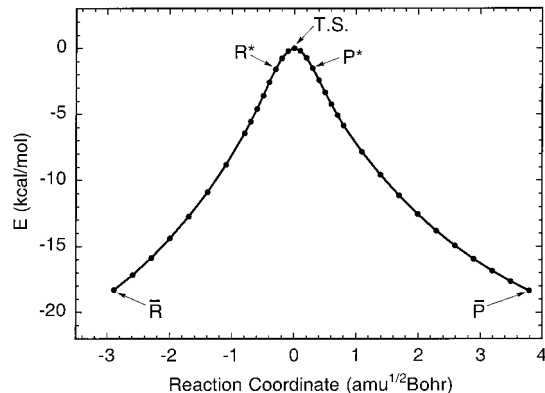

Figure 9. A portion of the minimum energy path for hydride transfer calculated with the RHF/3-21G method. The three points corresponding to structures R*, T. S., and P* are indicated. The points $\bar{R}$ and $\bar{P}$ used to generate the straight-line reaction path are also labeled.

structure is 0.22 kcal/mol (which is identical to that found for the one-dimensional hydrogen wavefunctions). As for the one-dimensional wavefunctions, these three-dimensional wavefunctions suggest that hydride tunneling is not significant along the MEP but is significant along the straight-line reaction path.

The RHF/3-21G method has been shown to give more accurate structures and energies than the PM3 method. Due to the computational expense, we generated only the portion of the MEP at the RHF/3-21G level shown in Figure 9. For comparison, the energies of the optimized reactant and product structures are −43.2 kcal/mol and −38.0 kcal/mol, respectively, relative to the T. S. energy. Note that this MEP is more symmetric than the MEP at the PM3 level.

Figure 10 depicts the hydride potential energy curves and the corresponding hydrogen vibrational wavefunctions for the
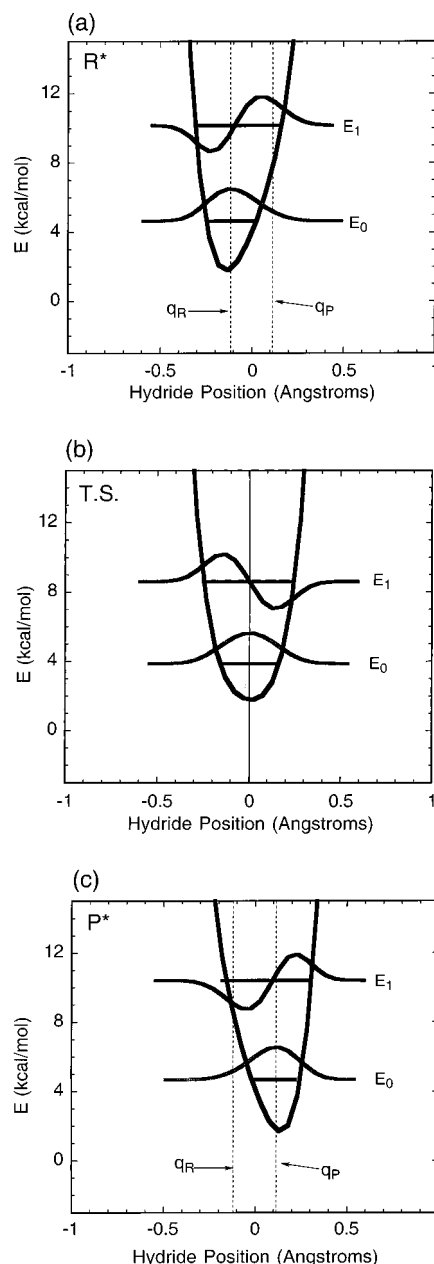

Figure 10. One-dimensional hydride potential energy curves obtained at the RHF/3-21G level and the corresponding one-dimensional hydrogen vibrational wavefunctions for the (a) R*, (b) T. S., and (c) P* structures defined in Figure 9. Both the ground and first excited hydride vibrational wavefunctions with energies E_0 and E_1, respectively, are shown. The dashed vertical lines in (a) and (c) denote the hydride coordinates q_R and q_P, where q_R represents the position of the projected classical hydride in R* and q_P represents the position of the projected classical hydride in P*. The solid vertical line in (b) indicates the position of the projected classical hydride in the T. S. structure.

RHF/3-21G structures R*, T. S., and P* along the MEP. The corresponding zero point energies are given in Table 1. Similar to the PM3 results, the RHF/3-21G hydride potential energy curves for the R* and P* structures are single wells with minima near C_D and C_A, respectively. In contrast to the PM3 results, however, the RHF/3-21G hydride potential energy curve for the transition state structure does not exhibit a barrier. This discrepancy between the PM3 and RHF/3-21G results does not lead to different overall conclusions for the two levels of theory, however, since the PM3 barrier at the transition state is very small. Thus, both levels of theory suggest that the hydride
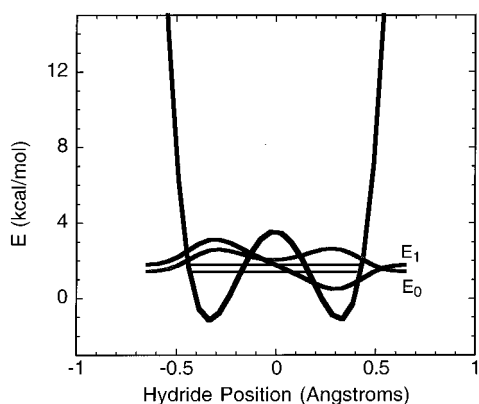
Figure 11. One-dimensional hydride potential energy curve obtained at the RHF/3-21G level and the corresponding one-dimensional hydrogen vibrational wavefunctions for a point along the straight-line reaction path connecting structures $\bar{R}$ and $\bar{P}$ denoted in Figure 9. The point was chosen so that the hydride potential energy curve is symmetric. Both the ground and first excited hydride vibrational wavefunctions with energies E_0 and E_1, respectively, are shown.

transfer reaction is vibrationally adiabatic and hydride tunneling is not significant along the MEP. We also observed that the frequency of the hydride potential energy curve for the transition state is significantly higher and the shoulders in the hydride potential energy curves for the R* and P* structures are less pronounced for RHF/3-21G than for PM3. These differences reflect the limitations of PM3, namely, that it does not describe partial double bonds and partially conjugated rings well since it was parametrized for minimum energy structures. In addition, although the classical hydride is not located exactly at the center of the hydrogen vibrational wavefunction for RHF/3-21G, the agreement is better than for PM3. This observation suggests that the inclusion of the nuclear quantum behavior of the hydride in the generation of the MEP would affect the MEP less for RHF/3-21G than for PM3.

The hydride potential energy curve and the corresponding hydrogen wavefunction at a point along the straight-line reaction path connecting structures $\bar{R}$ and $\bar{P}$ are depicted in Figure 11. The structures $\bar{R}$ and $\bar{P}$ correspond to the points denoted in Figure 9 and have C_D-C_A distances of 2.93 and 3.03 Å, respectively. The point along the associated straight-line reaction path depicted in Figure 11 was chosen so that the hydride potential energy curve was symmetric. For this structure, the C_D-C_A distance is 2.98 Å, which is significantly longer than the C_D-C_A distance of 2.59 Å for the transition state along the MEP. As for PM3, since the longer C_D-C_A distance leads to a higher barrier along the hydride coordinate, the lowest two vibrational states are below the barrier. In this case, the tunnel splitting is 0.36 kcal/mol and is expected to decrease as the C_D-C_A distance increases. Thus, nonadiabatic effects and hydride tunneling are expected to play important roles for this straight-line reaction path. Again, we emphasize that this specific straight-line reaction path is arbitrary and is merely an example of a reasonable alternative to the MEP. (Due to concerns that for a C_D-C_A distance of ~3.0 Å the closed shell single configuration RHF method may not be qualitatively correct for the whole range of relevant hydride positions, we also performed a two configuration self-consistent-field calculation for this structure. No configurational mixing occurred, suggesting that the RHF method provides a qualitatively correct description.)

Another goal of our calculations was to identify the dominant contributions to the reaction coordinate for various regions of the MEP. In general, the reaction coordinate along the MEP is a mixture of the hydride coordinate and other coordinates in

TABLE 2: Relevant RHF/3-21G Geometrical Values for the Following Structures: Reactant (R), R*, Transition State (T.S.), P*, and Product (P)[a]

	R	R*	T.S.	P*	P
C_D-C_A	3.74 Å	2.59 Å	2.59 Å	2.59 Å	4.18 Å
C_D-H-C_A	87.9°	167.9°	167.9°	167.7°	123.1°
$Zn-O$	1.88 Å	1.92 Å	1.93 Å	1.93 Å	1.92 Å
$O-H_{Ser48}$	1.38 Å	1.67 Å	1.69 Å	1.70 Å	3.56 Å
δ_1	$-36.1°$	$-25.1°$	$-21.2°$	$-16.9°$	8.6°
δ_2	181.3°	161.4°	157.9°	154.7°	138.3°
α_C	1.0°	11.8°	13.0°	14.0°	14.2°
α_N	0.4°	7.4°	7.6°	7.8°	10.7°

[a] R* and P* are defined in Figure 9, the angles δ_1, δ_2, α_C, and α_N are defined in Figure 12, and C_D and C_A represent the donor and acceptor carbons, respectively.
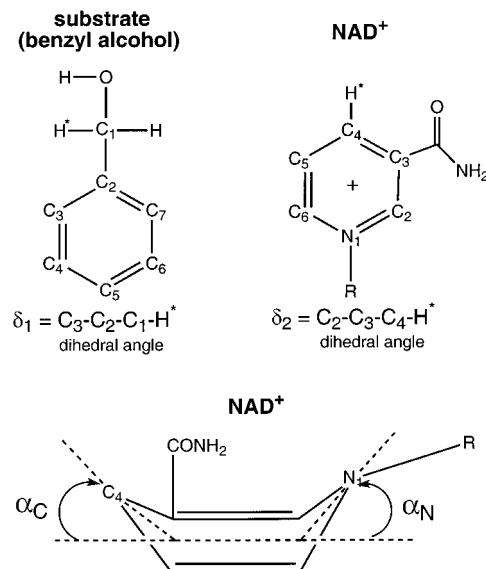

Figure 12. Definition of angles used in the text and tables.

the system. These other coordinates modulate the asymmetry of the hydride potential energy curve and induce hydride transfer by symmetrizing this potential. For the hydride transfer reaction studied in this paper, the region of the MEP in which this symmetrization occurs is between R* and P*. Figure 10 illustrates that the minimum of the hydride potential energy curve is shifted from q_R to q_P between R* and P*. As a result, the hydrogen vibrational wavefunction shifts from the C_D side to the C_A side between R* and P*.

We performed a structural analysis along the MEP to determine the major contributions to the reaction coordinate. The relevant geometrical values for the reactant (R), R*, T. S., P*, and product (P) structures are given in Table 2. Note that the $Zn-O$, C_D-C_A, and $O-H_{Ser48}$ are all virtually the same for the R* and P* structures. Thus, they do not contribute significantly to the reaction coordinate in the region between R* and P*. On the other hand, the C_D-C_A and $O-H_{Ser48}$ distances change substantially in the regions between R and R* and between P* and P and thus contribute to the reaction coordinate in these regions. The most significant structural differences between R* and P* are the angles δ_1 and δ_2 of the secondary hydrogen atoms and the angles α_C and α_N measuring the degree of puckering in the NAD$^+$ ring. These angles, which are defined in Figure 12, also contribute to the reaction coordinate between R and R* and between P* and P. (Note that the values obtained for α_C and α_N are similar to those studied by Bruice and co-workers[27] and by Houk and co-workers[28] on smaller model systems.) We investigated the roles

Calculation of Hydrogen Vibrational Wavefunctions

J. Phys. Chem. B, Vol. 104, No. 37, 2000 **8891**

of both the secondary hydrogen atoms and the puckering of the NAD$^+$ ring along the MEP for the hydride transfer reaction.

The contribution of the secondary hydrogens to the reaction coordinate near the transition state indicates significant coupling between the secondary hydrogens and the transferring hydride. In the FGH-MCSCF approach, all nuclei except the transferring hydride are fixed during the calculation of the hydride potential and the corresponding hydrogen vibrational wavefunctions. In other words, the hydride is assumed to respond instantaneously to the positions of the other nuclei. This adiabatic separation is invalid if other nuclear coordinates move on a similar time scale as the hydride. For example, the secondary hydrogen atoms are expected to move on a similar time scale as the transferring hydride. A rigorous treatment would require calculating a multidimensional wavefunction including the motion of the secondary hydrogen atoms and the transferring hydride. Currently, this treatment is computationally prohibitive due to the expense of calculating the potential on a multidimensional grid (i.e., 9-dimensional if all three hydrogen atoms are treated in three dimensions).

To investigate the error introduced by this adiabatic separation, we studied the opposite adiabatic limit, where the secondary hydrogens are assumed to respond instantaneously to the position of the transferring hydride. This calculation involved allowing these two hydrogen atoms to relax at each grid point of the hydride potential energy curve. The resulting "relaxed" hydride potential energy curves are shown together with the original hydride potential energy curves in Figure 13. Clearly, the frequencies are smaller (i.e., shallower wells) for the relaxed curves, but the minima have not shifted significantly. Thus, the secondary hydrogen coordinates are not the dominant modes responsible for the shifting of the hydrogen vibrational wavefunction between R* and P*. Moreover, although a very small barrier appears for the transition state hydride potential energy curve, the lowest-energy hydride vibrational state would be above this small barrier and delocalized between the donor and acceptor carbon atoms, as in the unrelaxed case shown in Figure 10. Thus, the secondary hydrogen atoms do not appear to induce significant tunneling of the transferring hydride or vibrational nonadiabaticity along the MEP. The multidimensional quantum treatment of all three hydrogen atoms mentioned above is a direction for the future. In any case, these calculations indicate that the secondary hydrogens are not primarily responsible for the shift of the hydride wavefunction between R* and P*.

As shown in Table 2, the other significant structural difference between the R* and P* structures is the puckering of the NAD$^+$ ring. We performed an LMO analysis to investigate the electronic effects induced by this ring puckering mode. As shown in Figure 10, the minimum of the hydride potential energy curve is at q_R for R* and q_P for P*. In other words, the energy at q_R is less than the energy at q_P for the R* structure, whereas the reverse is true for the P* structure. To elucidate the fairly subtle electronic differences between these two structures, we studied the LMOs for each structure with the hydride at both q_R and q_P.

Figure 14 depicts the LMOs for the R* structure. The first column depicts the LMOs with the hydride at q_R, whereas the second column depicts them with the hydride at q_P. Figures 14a−d depict the LMOs representing the C_D−O bond. When the hydride is at q_R, one of these LMOs represents a C_D−O σ bond (a) and the other represents the early stages of a C_D−O π bond (c). When the hydride is at q_P, the corresponding LMOs in (b) and (d) exhibit slightly more π character. This difference can be explained by Figures 14e and 14f, which depict the
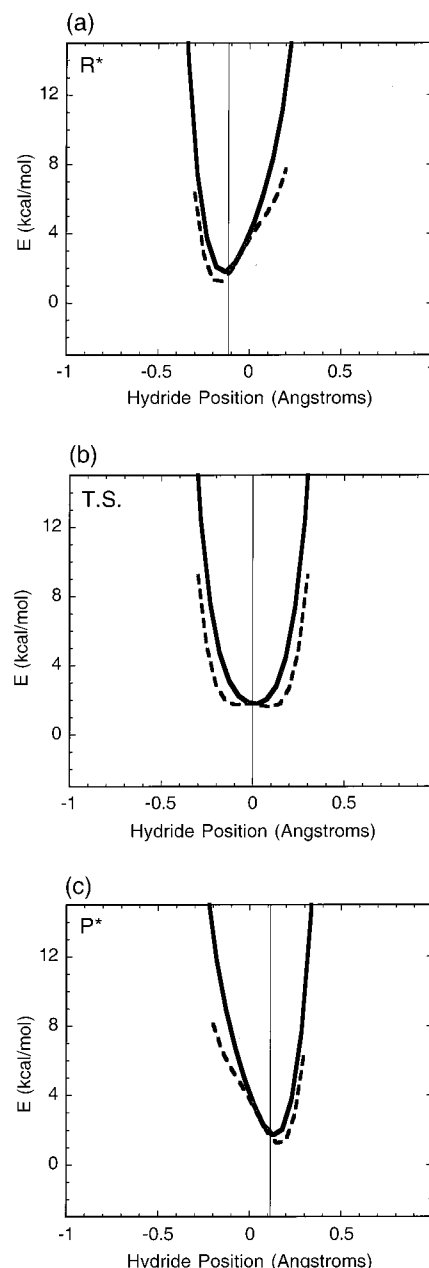

Figure 13. One-dimensional hydride potential energy curves obtained at the RHF/3-21G level for the (a) R*, (b) T. S., and (c) P* structures defined in Figure 9. The curves are depicted for the standard method with the secondary H atoms frozen (solid) and for the modified method allowing the secondary H atoms to relax for each grid point along the one-dimensional hydride coordinate (dashed). The vertical lines indicate the positions of the projected classical hydride.

LMOs representing the two-electron three-center C_D−H−C_A bond. These LMOs suggest that electron density is shifted from C_D to C_A when the hydride is moved from q_R to q_P. This electron density shift leads to the greater π character of the C_D−O bond when the hydride is at q_P. Figures 14g−j depict the LMOs representing the C_2−C_3 bonds in the NAD$^+$ ring (where the carbons are labeled as in Figure 12). Note that this double bond is conjugated to the C_A carbon to a greater extent when the hydride is at q_R [(g) and (i)] than when the hydride is at q_P [(h) and (j)]. The greater conjugation when the hydride is at q_R is most likely due to the smaller electron density near C_A, as suggested by the three-center two-electron LMO in Figure 14e relative to that in Figure 14f. We also observed similar behavior for the LMOs representing the C_5−C_6 bond in the NAD$^+$ ring.
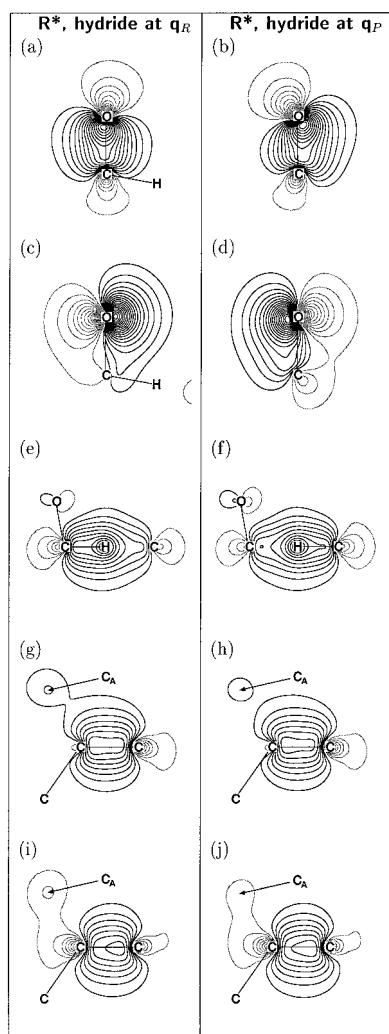
Figure 14. Localized molecular orbitals obtained at the RHF/3-21G level for the R* structure. The left and right columns depict LMOs for the hydride at q_R and q_P, respectively. The LMOs are identified as follows: (a)−(d) represent the C_D−O bonds; (e) and (f) represent a two-electron, three center C_D−H−C_A bond; and (g)−(j) represent the C_2−C_3 bonds in the NAD$^+$ ring. The contour increments are 0.05 Bohr$^{3/2}$. The position of C_A is indicated with an arrow.

We conclude that the energy of R* is lower when the hydride is at q_R than when the hydride is at q_P in part because the smaller electron density at C_A when the hydride is at q_R leads to greater conjugation within the NAD$^+$ ring.

Figure 15 depicts the LMOs for the P* structure. The first column depicts the LMOs with the hydride at q_P, whereas the second column depicts them with the hydride at q_R. Figure 15a−d depict the LMOs representing the C_D−O bond. When the hydride is at q_P, the two LMOs in (a) and (c) represent an almost completely formed double C_D−O bond (i.e., two nearly equivalent LMOs including both σ and π character). When the hydride is at q_R, one of these LMOs represents a C_D−O σ bond (b) and the other represents the early stages of a C_D−O π bond (d). This difference can be explained by Figure 15e and 15f, which depict the LMOs representing the two-electron three-center C_D−H−C_A bond. Again, the shift of electron density from C_D to C_A as the hydride moves from q_R to q_P allows the C_D−O bond to have more π character when the hydride is at q_P. Figures 15g−j depict the LMOs representing the C_2−C_3 bonds in the NAD$^+$ ring. In contrast to the R* structure, there is no conjugation of this double bond to the ring due to the larger puckering of the NAD$^+$ ring. These bonds are virtually identical
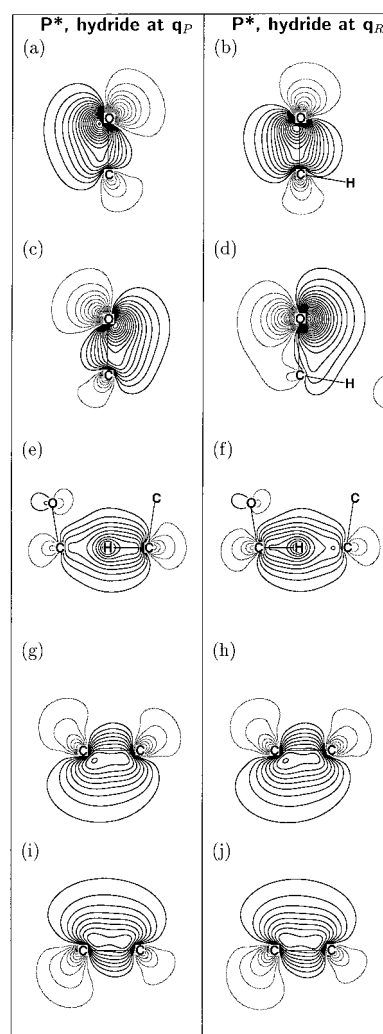

Figure 15. Localized molecular orbitals obtained at the RHF/3-21G level for the P* structure. The left and right columns depict LMOs for the hydride at q_P and q_R, respectively. The LMOs are identified as follows: (a)−(d) represent the C_D−O bonds; (e) and (f) represent the two-electron, three center C_D−H−C_A bonds; and (g)−(j) represent the C_2−C_3 bonds in the NAD$^+$ ring. The contour increments are 0.05 Bohr$^{3/2}$.

when the hydride is at q_R and when the hydride is at q_P. We conclude that the energy of P* is higher when the hydride is at q_R than when the hydride is at q_P in part because the smaller electron density at C_A when the hydride is at q_R leads to an electron-deficient C_A that is unable to recover any electron density through conjugation to the NAD$^+$ ring due to puckering of the ring.

We also observed that the C_D−O bonding is qualitatively different for the R* structure with the hydride at q_P than for the P* structure with the hydride again at q_P. In the P* case, the C_D−O π system is completely formed (two equivalent LMOs); in the R* case, the π system is only partially formed (compare Figures 14b and 14d to Figures 15a and 15c). This difference and the explanation for it suggests why the R* structure with the hydride at q_P is much higher in energy than the P* structure with the hydride at q_P. For the P* system, there is no conjugation of the NAD$^+$ ring to C_A, so it is able to accept a significant amount of electron density from the C_D−H−C_A bond, leading to a depletion in electron density around C_D. In turn, this allows replacement of the electron density around C_D through the full formation of the C_D−O π bond. For the R* case, there is ring conjugation to C_A, which results in added electron density

Calculation of Hydrogen Vibrational Wavefunctions

J. Phys. Chem. B, Vol. 104, No. 37, 2000 **8893**

around C_A, so it is unable to accept as much electron density from the C_D-H-C_A bond and the depletion of electron density near C_D is not as great (compare Figures 14f and 15e). In turn, this prevents the full formation of a C_D-O π bond and leads to an overall bonding arrangement that is energetically unfavorable.

To summarize the LMO analysis, we found that the shifting of the hydride potential energy curves for the R* and P* structures is due mainly to the greater puckering of the NAD^+ ring for the P* structure compared to the flattening of the ring for the R* structure. The greater puckering for the P* structure diminishes the conjugation in the ring, which removes electron density from C_A to other parts of the ring. This renders the increase of electron density from the C_D-H-C_A bond near C_A more favorable than near C_D. In contrast, the enhanced level of conjugation in the flatter NAD^+ ring for the R* structure adds electron density to C_A from other parts of the ring. This renders the increase of electron density from the C_D-H-C_A bond near C_D more favorable than near C_A. Thus, the critical difference between R* and P* is the puckering of the NAD^+ ring, which determines the electron density at C_A, which in turn dictates the most favorable location of the electron density within the C_D-H-C_A bond. This difference shifts the localization of the hydrogen vibrational wavefunctions from C_D to C_A as the structure changes from R* to P*.

IV. Conclusions

This paper presents an application of an approach combining electronic structure methods with hydrogen vibrational wavefunction calculations. This approach centers on the analysis of the hydrogen vibrational wavefunctions, as well as the geometries and electronic molecular orbitals, along reaction paths obtained with electronic structure methods. We have illustrated that this approach provides valuable insight into the fundamental nature of the nuclear quantum effects, including the significance of hydrogen tunneling and zero point energy, the role of secondary hydrogens, and the dominant contributions to the reaction coordinate. We have shown that the nuclear quantum effects may be qualitatively different along straight-line reaction paths than along minimum energy paths.

The application of this approach to a model system representing the hydride transfer step of the LADH-catalyzed oxidation of benzyl alcohol has elucidated the nature of the nuclear quantum effects in this reaction. Our results suggest that the hydride transfer is adiabatic (i.e., remains in the ground hydrogen vibrational state) and that hydride tunneling (i.e., hydride transfer through a barrier) does not play a critical role along the MEP due to the absence of a significant barrier along the hydride coordinate. On the other hand, we found that nonadiabatic effects and hydride tunneling are significant for straight-line reaction paths generated from points on the MEP. These straight-line reaction paths are expected to be more relevant for hydride transfer reactions.[15,16] Moreover, experimental results indicating hydride tunneling in LADH[2] support the relevance of the straight-line reaction paths.

We also investigated the dominant contributions to the reaction coordinate along the reaction paths. We found that the secondary hydrogens are coupled to the hydride near the transition state, as supported by the significant secondary kinetic isotope effects measured experimentally in LADH.[2] In addition, a localized molecular orbital analysis allowed us to determine that the puckering of the NAD^+ ring is a vital contribution to the reaction coordinate near the transition state since this puckering motion shifts the hydrogen vibrational wavefunction from the donor side to the acceptor side. Further from the

transition state, the reaction coordinate is a mixture of many heavy-atom modes, including the donor−acceptor distance and the distance between the alkoxide oxygen and the neighboring Ser48. As a result, the straight-line reaction paths involve significantly larger distances between the donor and acceptor carbon atoms, leading to a higher and wider barrier along the hydride coordinate.

These calculations elucidate the factors influencing hydrogen tunneling in LADH. We found that the puckering of the NAD^+ ring modulates the asymmetry of the hydride potential energy curve and induces hydride transfer by symmetrizing this potential. In addition, we found that increasing the distance between the donor and acceptor carbon atoms increases the height and width of the barrier along the hydride coordinate. The height and width of this barrier determine the tunnel splitting, which in turn determines the extent of hydrogen tunneling. Thus, our calculations imply that hydrogen tunneling in LADH is strongly impacted by both the puckering of the NAD^+ ring (which modulates the asymmetry of the hydride potential energy curve) and the distance between the donor and acceptor carbons (which modulates the barrier of the hydride potential energy curve). The dependence of hydrogen tunneling on the distance between the donor and acceptor carbon atoms in LADH has also been shown experimentally through the investigation of a series of mutants.[29]

Although these studies have provided useful insight into the nuclear quantum effects for this model system, the quantitative accuracy could be improved in a number of ways. The remainder of the enzyme, as well as solvent molecules, must be included for a more realistic description. In addition, a higher level of theory should be used: the PM3 method has been shown to be of limited accuracy in terms of both geometries and energies, and the RHF/3-21G method has been shown to provide reliable structures but only qualitatively accurate energies for this system.[12] Furthermore, our results indicate that the secondary hydrogens are coupled to the hydride, so a complete study requires the calculation of multidimensional hydrogen vibrational wavefunctions including the secondary hydrogens as well as the hydride. Finally, we neglected the dynamical effects that will significantly impact this reaction. Note that these limitations are not expected to alter the qualitative conclusions discussed above.

Our approach, combining electronic structure methods with hydrogen vibrational wavefunction calculations, provides the foundation for future methodological developments. To avoid the difficulties in determining the relevant reaction path, we are developing methodology in which the transferring hydrogen nucleus is treated quantum mechanically with molecular orbital methods on equal footing with the electrons. The reaction coordinate for the MEP generated with this new methodology will not include the transferring hydrogen nucleus and thus should not exhibit the large curvature associated with hydrogen transfer reactions. To include dynamical effects, we will utilize mixed quantum/classical molecular dynamics methodology in which the transferring hydrogen nucleus is treated quantum mechanically while the remaining nuclei are treated classically. In this molecular dynamics methodology, the classical nuclei move according to a potential derived from the quantum mechanical wavefunction. Surface hopping methods may be used to describe the feedback between the quantum and classical subsystems.[29] These exciting developments will provide even more insight into systems such as LADH.

8894 *J. Phys. Chem. B, Vol. 104, No. 37, 2000*

Webb et al.

References and Notes

(1) Cha, Y.; Murray, C. J.; Klinman, J. P. *Science* **1989**, *243*, 1325.

(2) Bahnson, B. J.; Park, D.-H.; Kim, K.; Plapp, B. V.; Klinman, J. P. *Biochemistry* **1993**, *32*, 5503.

(3) Bahnson, B. J.; Colby, T. D.; Chin, J. K.; Goldstein, B. M.; Klinman, J. P. *Proc. Natl. Acad. Sci.* **1997**, *94*, 12797. Colby, D. C.; Bahnson, B. J.; Chin, J. K.; Klinman, J. P.; Goldstein, B. M. *Biochemistry* **1998**, *37*, 9295.

(4) Bahnson, B. J.; Klinman, J. P. *Methods Enzymol.* **1995**, *249*, 374.

(5) Kohen, A.; Klinman, J. P. *Acc. Chem. Res.* **1998**, *31*, 397.

(6) Kreevoy, M. M.; Ostovic, D.; Lee, I.-S. H.; Binder, D. A.; King, G. W. *J. Am. Chem. Soc.* **1988**, *110*, 524.

(7) Kim, Y.; Truhlar, D. G.; Kreevoy, M. M. *J. Am. Chem. Soc.* **1991**, *113*, 7837.

(8) Yadav, A.; Jackson, R. M.; Holbrook, J. J.; Warshel, A. *J. Am. Chem. Soc.* **1991**, *113*, 4800.

(9) Hwang, J.-K.; Chu, Z. T.; Yadav, A.; Warshel, A. *J. Phys. Chem.* **1991**, *95*, 8445.

(10) Bruno, W. J.; Bialek, W. *Biophys. J.* **1992**, *63*, 689.

(11) Rucker, J.; Klinman, J. P. *J. Am. Chem. Soc.* **1999**, *121*, 1997.

(12) Agarwal, P. K.; Webb, S. P.; Hammes-Schiffer, S. *J. Am. Chem. Soc.* **2000**, *122*, 4803.

(13) Ando, K.; Hynes, J. T. *J. Phys. Chem. B* **1997**, *101*, 10464.

(14) Truhlar, D. G.; Isaacson, A. D.; Garrett, B. C. *Theory of Chemical Reaction Dynamics*, Baer, M., Ed.; CRC Press: Boca Raton, FL, 1985; Vol. 4.

(15) Miller, W. H.; Ruf, B. A.; Chang, Y.-T. *J. Chem. Phys.* **1988**, *89*, 6298.

(16) Garrett, B. C.; Joseph, T.; Truong, T. N.; Truhlar, D. G. *Chem. Phys.* **1989**, *136*, 271.

(17) Binkley, J. S.; Pople, J. A.; Hehere, W. J. *J. Am. Chem. Soc.* **1980**, *102*, 939.

(18) Gordon, M. S.; Binkley, J. S.; Pople, J. A.; Pietro, W. J.; Hehre, W. J. *J. Am. Chem. Soc.* **1983**, *104*, 2797.

(19) Dobbs, K. D.; Hehre, W. J. *J. Comput. Chem.* **1987**, *8*, 861.

(20) Gonzales, C.; Schlegel, H. B. *J. Chem. Phys.* **1989**, *90*, 2154.

(21) Boys, F. S. *The Quantum Theory of Atoms, Molecules and Solids*; Academic Press: New York, 1966.

(22) Schmidt, M. W.; Baldridge, K. K.; Boatz, J. A.; Elbert, S. T.; Gordon, M. S.; Jensen, J. H.; Koseki, S.; Matsunaga, N.; Nguyen, K. A.; Su, S.; Windus, T. L.; Dupuis, M.; Montgomery, J. A. *J. Comput. Chem.* **1993**, *14*, 1347.

(23) Gaussian 98, Revision A.6, Frisch, M. J.; Trucks, G. W.; Schlegel, H. B.; Scuseria, G. E.; Robb, M. A.; Cheeseman, J. R.; Zakrzewski, V. G.; Montgomery, J. A., Jr.; Stratmann, R. E.; Burant, J. C.; Dapprich, S.; Millam, J. M.; Daniels, A. D.; Kudin, K. N.; Strain, M. C.; Farkas, O.; Tomasi, J.; Barone, V.; Cossi, M.; Cammi, R.; Mennucci, B.; Pomelli, C.; Adamo, C.; Clifford, S.; Ochterski, J.; Petersson, G. A.; Ayala, P. Y.; Cui, Q.; Morokuma, K.; Malick, D. K.; Rabuck, A. D.; Raghavachari, K.; Foresman, J. B.; Cioslowski, J.; Ortiz, J. V.; Stefanov, B. B.; Liu, G.; Liashenko, A.; Piskorz, P.; Komaromi, I.; Gomperts, R.; Martin, R. L.; Fox, D. J.; Keith, T.; Al-Laham, M. A.; Peng, C. Y.; Nanayakkara, A.; Gonzalez, C.; Challacombe, M.; Gill, P. M. W.; Johnson, B.; Chen, W.; Wong, M. W.; Andres, J. L.; Gonzalez, C.; Head-Gordon, M.; Replogle, E. S.; Pople, J. A.; *Gaussian 98*, Revision A.6; Gaussian, Inc.: Pittsburgh, PA, 1998.

(24) Webb, S. P.; Hammes-Schiffer, S. *J. Chem. Phys.*, in press.

(25) Marston, C. C.; Balint-Kurti, G. G. *J. Chem. Phys.* **1989**, *91*, 3571.

(26) Shearer, G. L.; Kim, K.; Lee, K. M.; Wang, C. K.; Plapp, B. V. *Biochemistry* **1993**, *32*, 11186.

(27) Almarsson, Ö.; Bruice, T. C. *J. Am. Chem. Soc.* **1993**, *115*, 2125.

(28) Wu, Y.-D.; Houk, K. N. *J. Am. Chem. Soc.* **1991**, *113*, 2353.

(29) Hammes-Schiffer, S. *J. Phys. Chem. A* **1998**, *102*, 10443.